J. Fluid Mech. (2004), *vol.* 516, *pp.* 239–264.
DOI: 10.1017/S0022112004000667 Printed in the United Kingdom

Length scales in wall-bounded high-Reynolds-number turbulence

By PIERRE CARLOTTI[1] AND PHILIPPE DROBINSKI[2]

[1]Centre d'Étude des Tunnels, Bron, France
Pierre.Carlotti@equipement.gouv.fr

[2]Institut Pierre Simon Laplace/Service d'Aéronomie, Paris, France

(Received 20 January 2004 and in revised form 18 May 2004)

In this study, estimates of inhomogeneous integral scales are derived from rapid distortion theory (RDT) for the case of wall-bounded high-Reynolds-number turbulence and from large-eddy simulation (LES) of a neutrally stratified atmospheric boundary layer (ABL). As for any inhomogeneous flow, integral scales in different directions are introduced. Downward integral scales are introduced since they differ from the usual vertical integral scales because of the presence of the wall. The study concentrates on the length scales based on the vertical velocity, which are the most affected by blocking by the wall, which is assumed to be horizontal.

It is shown from RDT that the asymptotic behaviour of the integral length scales for small heights depends crucially on the spectrum power law $-2p$. When $2p > 1$ there is always one length scale which does not scale with the distance to the wall z. Only the downward integral scale is proportional to z for any $2p$. These results show that the assumption, often made in studies of boundary layers, that all the lengths are proportional to z, is not compatible with the assumption of a spectrum decaying according to Kolmogorov's law, but rather with a spectrum following a -1 power law. It is an encouraging result since there is now widespread theoretical, experimental and numerical evidence that such a -1 power-law subrange exists in the spectra of high-Reynolds-number wall-bounded turbulence, for eddies larger than z. The RDT results allow an interpretation of the vertical profiles of the integral length scales computed from the LES outputs: above the third grid point, the vertical profiles of the integral length scales have a linear shape, as expected for high-Reynolds-number turbulence and $2p = 1$. Very close to the surface, the upward integral length scales decreases with z because of the fast decay of the spectrum ($2p > 2$) from the LES subgrid model.

The longitudinal-to-transverse integral length scale ratio is computed using RDT and LES. This ratio is interpreted as the aspect ratio of elongated near-wall large eddies, which are ubiquitous features of LES of boundary layers in which shear plays an important role in the dynamics. The LES shows that the longitudinal-to-transverse integral length scale ratio is an increasing function of z, ranging between 1 and 3, which is of the order of magnitude of the published theoretical value of 3.5. From RDT, the evolution with z of the longitudinal-to-transverse integral length scale ratio means either that the velocity shear β decreases with z and the spectral power law $2p$ varies in a non-trivial manner, or if both the RDT and LES are valid that the scale of the large eddies is proportional to βz with β varying from 1.3 to about 4.

1. Introduction

Turbulence can be characterized by two types of length scale, following Hunt *et al.* (1989), *functional* length scales and *integral* length scales. Functional length scales are the ratios of two statistical quantities of the flow, where the ratio has the dimension of a length. They are generally derived from one-point quantities (Andrén & Moeng 1993). Functional length scales are very often used in turbulence modelling because they can be computed relatively easily, using only the values of one-point quantities. The most relevant functional length scale at very high Reynolds number is the dissipation scale $\mathscr{L}_\varepsilon = E^{3/2}/\varepsilon$, where $E = (1/2)(\overline{u_i^2})^{1/2}$ is the total turbulent kinetic energy (where u_1, u_2 are the turbulent horizontal velocity components and u_3 the vertical velocity) and $\varepsilon = \mathrm{d}E/\mathrm{d}t$ the dissipation.

On the other hand, integral length scales are obtained from the shape of the two-point correlation curve of a quantity in the flow or other non-local properties. Theoretical studies usually rely on two-point quantities, which are easier to interpret theoretically. Other length scales are used in turbulence studies: Kolmogorov's length $\eta_K = (\nu^3/\varepsilon)^{1/4}$ (ν being the molecular viscosity), which is a functional length scale, and Taylor's microscale, which is actually an integral length for some authors (e.g. Batchelor 1953, p. 47) and a functional length for others (Frisch 1995). Neither Kolmogorov's nor Taylor's lengths are considered in the present paper, because they tend to 0 as the Reynolds number increases. In atmospheric problems, they are several orders of magnitude smaller than the lengths of interest, typically of order millimetres compared to lengths of order metres to kilometres considered here.

In homogeneous turbulence, it can be shown that $\mathscr{L}_\varepsilon$ and the integral scale L^H are proportional. Assume that turbulence follows a Kármán spectrum (Hunt & Graham 1978),

$$E(k) = \left(\frac{55}{9}\alpha_K\right)\frac{\varepsilon^{2/3}k^4}{\left(g_2 L_0^{-2} + k^2\right)^{17/6}} \quad \text{with } \alpha_K \approx 0.25,\ g_2 = 0.558$$

where L_0 is a length and k the wavenumber. A Kármán spectrum is in general a good fit of atmospheric data at intermediate heights (Mann 1994). Then $\mathscr{L}_\varepsilon$ and L^H can be computed as functions of L_0 only, $\mathscr{L}_\varepsilon \approx 2.65L_0$ and $L^H \approx 2.38L_0$. This proportionality reflects one of the fundamental ideas of turbulence: the universality of homogeneous turbulent flows means that only one length scale is sufficient to characterize the flow. On the other hand, the problem is much more complicated in inhomogeneous turbulence.

In this case, several inhomogeneous integral scales can be introduced, generalizing the ideas of Hunt *et al.* (1989), Lee & Hunt (1989) and Jacquin *et al.* (1990):

$$L_{ij}^{(x_k+)} = \frac{\displaystyle\int_0^\infty \overline{u_i(\boldsymbol{x})u_j(\boldsymbol{x}+r\boldsymbol{e}_k)}\,\mathrm{d}r}{\overline{u_i u_j}}, \qquad (i,j,k) \in \{1,2,3\}^3 \tag{1.1}$$

where x_k are the geometrical coordinates (x_3 or z being the vertical coordinate) (see figure 1). These eighteen length scales take into account all directions of velocity and separation. In strongly inhomogeneous turbulence, they may all be different. However, in the case of the atmospheric boundary layer or of any turbulent flow bounded by a flat surface, they do not take into account the presence of this flat surface. This

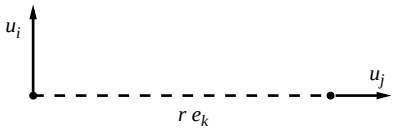

FIGURE 1. Definition of the integral scales.

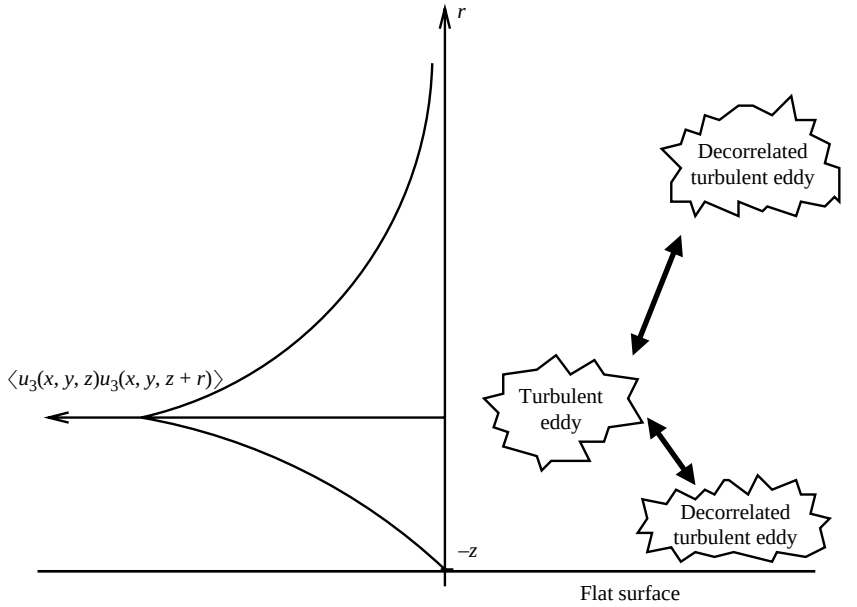

FIGURE 2. Qualitative sketch of the difference between the downward and upward integral scales.

suggests introducing the integral scales

$$L_{ij}^{(z-)} = \frac{\displaystyle\int_0^z \overline{u_i(\boldsymbol{x})u_j(\boldsymbol{x} - r\boldsymbol{e}_3)}\,\mathrm{d}r}{\overline{u_i u_j}}, \qquad (i, j) \in \{1, 2, 3\}^2. \tag{1.2}$$

In the following, $L_{ij}^{(z-)}$ is called the vertical *downward* integral scale, and $L_{ij}^{(z+)}$ the vertical *upward* integral scale. Taking points at different heights, (x, y, z) and (x, y, z'), and writing $r = z' - z$, results in

$$\overline{u_i(x, y, z)u_j(x, y, z + r)} = \overline{u_i(x, y, z')u_j(x, y, z' - r)}.$$

Therefore, the integrand is similar in the definitions of $L_{ij}^{(z+)}$ and $L_{ij}^{(z-)}$, but not the limits of integrations, nor the location of the normalization variance, which is at the lower limit of integration for $L_{ij}^{(z+)}$ and at the upper limit of integration for $L_{ij}^{(z-)}$. A sketch explaining the differences is given in figure 2. These length scales will prove to be useful to characterize the *anisotropy of turbulence*.

Integral length scales are related to the spectra in the surface layer. For a moderate-Reynolds-number turbulent boundary layer, it was shown by Hunt & Carruthers

(1990) that the spectra display a k_1^{-2} subrange, which can be connected with the appearance of elongated streaks (Lin, Adrian & Hanratty 1996). For a high-Reynolds-number boundary layer, the situation is less clear. In the case of the atmospheric surface layer, Drobinski *et al.* (2004) showed that the surface layer can be divided into two sublayers: (i) the *eddy surface layer* (ESL) which is the lower sublayer where blocking of impinging eddies is the dominating mechanism (Hunt & Carlotti 2001) and where a k_1^{-1} subrange is visible on the longitudinal and transverse velocity fluctuation spectra only; (ii) the *shear surface layer* (SSL) which is an intermediate sublayer, where shear affects the isotropy of turbulence (Kader & Yaglom 1989; Yaglom 1991) and where a k_1^{-1} subrange is found in the spectra of the three velocity fluctuation components. However, Morrison *et al.* (2002) show a very interesting result from a pipe flow experiment apparently not displaying any k_1^{-1} range in the spectrum. Unfortunately, a careful comparison of the experimental conditions that do or do not give a k_1^{-1} range is still to be done.

The aim of the present study is to use a combination of two tools, inhomogeneous rapid distortion theory (RDT) and high-resolution large-eddy simulations (LES) to shed some light on integral scales in the neutral atmospheric boundary layer (ABL). Neither of these two tools can perfectly represent the actual boundary layer, because inhomogeneous RDT relies on several simplifications and assumptions and LES relies on subgrid models. The point of view adopted for the inhomogeneous RDT is to assume that the high-altitude spectrum has the shape of a general spectrum with decay rate $2p \geqslant 1$ to derive inhomogeneous integral length scales. For the LES, a classical subgrid model is used, but at a much higher resolution than usually in atmospheric studies, in order to minimize the influence of subgrid models. Inhomogeneous RDT and LES are used together in order to try to overcome their limitations.

The expressions for the inhomogeneous integral scales close to a wall are computed in § 2 using RDT. The high-resolution LES is described in § 3, and the results put in perspective and analysed in § 4. Section 5 looks at the results from the point of view of elongated large eddies ('streaks') and § 6 concludes this study.

2. Derivation and resolution of the shear and blocking equations using rapid distortion theory

2.1. *Rapid distortion theory*

In the context of the atmospheric boundary layer, RDT was introduced by Moffatt (1967) to take into account the effect of shear. It has been used by Townsend (1976) to compute theoretical estimates of Reynolds stresses. The possibility of taking into account the blocking of turbulence by the ground (i.e. the remote reduction of the vertical component of the velocity above the flat surface) was introduced by Hunt & Graham (1978) in the context of shear-free turbulence, and generalized by Lee & Hunt (1989) to consider the case of sheared and blocked turbulence. More recently, it was shown by Carlotti & Hunt (2003) that the use of RDT over a solid boundary can be understood as a mean of concisely describing the structure of turbulence, through a 'potential' spectrum.

In the atmospheric boundary layer, the mean shear varies with height. Therefore the RDT models, which all use a uniform value for the shear, could appear irrelevant (figure 3). However, in order to keep analytical simplicity, shear-free and uniform-shear

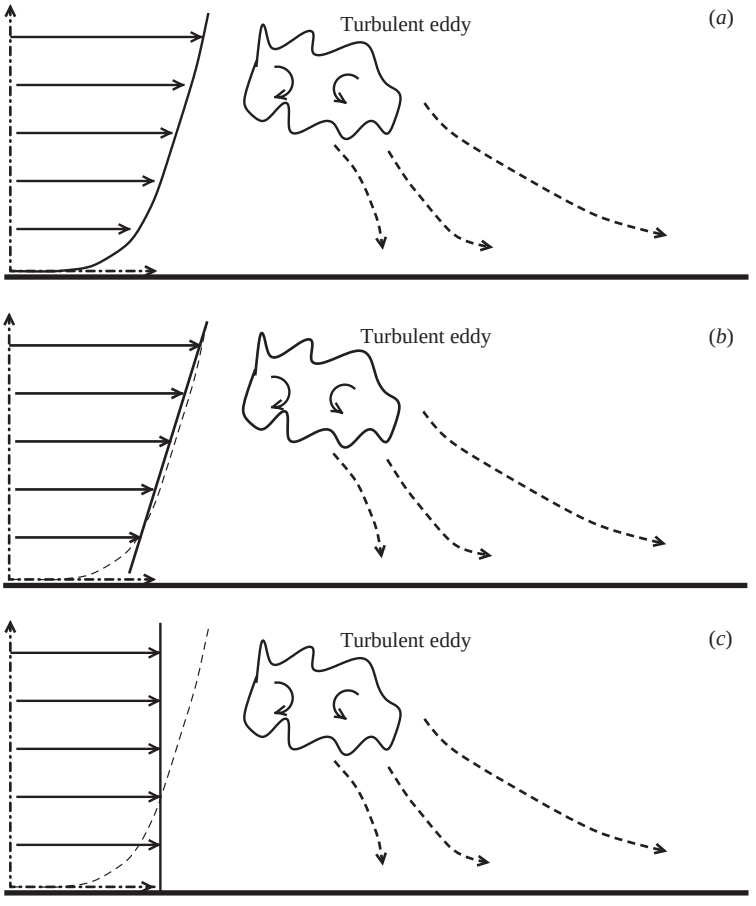

FIGURE 3. Simplified models for the atmospheric boundary layer; (*a*) non-uniform shear; (*b*) uniform shear; (*c*) no shear.

models will be used here, following Lee & Hunt (1989). These models are justified *a posteriori* by the agreement of their results with measurements, and, in the present case, with LES.

The shear flow has the form $(U_0+Sz, 0, 0)$ where U_0 is a constant and homogeneous background flow and S is a constant shear. We will consider a flow in the inviscid limit (see Hunt & Graham (1978) for a justification of taking the flow in the inviscid limit – see also Magnaudet (2003), who proved that Hunt & Graham's (1978) theory is a leading-order approximation capable of describing short- and long-term evolution of shear-free boundary layers in the limit of large Reynolds numbers, even though viscosity is neglected.) The boundary condition imposed by the blocking is then simply that the vertical component of the velocity field must be zero. The velocity field is decomposed into two components: the shear field, and the fluctuating field. More precisely, if we denote the velocity field as $\boldsymbol{U}$, we can use the decomposition $\boldsymbol{U} = (U_0 + Sz)\boldsymbol{e}_x + \boldsymbol{u}$. Then $\boldsymbol{u}$ will be identical to the fluctuation field as long as only linear processes are considered. In the same way, we note that $\boldsymbol{U}\cdot\nabla\boldsymbol{U} = 0$ because the streamlines of the flow $\boldsymbol{U} = (U_0+Sz, 0, 0)$ are parallel. Furthermore, if we assume S independent of z then $\nabla^2\boldsymbol{U} = 0$. The Navier–Stokes equations in our case take the

form

$$\left.\begin{aligned}\partial_t \boldsymbol{u} + (\boldsymbol{U}+\boldsymbol{u})\cdot\nabla(\boldsymbol{U}+\boldsymbol{u}) &= -\nabla p,\\ \nabla\cdot\boldsymbol{u} &= 0,\end{aligned}\right\} \tag{2.1}$$

where p is the pressure divided by the reference density. In order to evaluate the length scales introduced in the previous section, we use inhomogeneous RDT. RDT consists of (i) choosing an initial condition that is relevant and statistically known and (ii) linearizing the equations by neglecting the term $\boldsymbol{u}\cdot\nabla\boldsymbol{u}$. In the following, we consider a flow over a rigid plane $z = 0$ in the physical space. At $t < 0$, the velocity field (u_1^H, u_2^H, u_3^H) is supposed to be homogeneous. At $t = 0$, the blocking boundary condition and a shear flow are introduced.

The principle of the use of an unsteady theory, where the effective shear $\beta = St$ depends on time, in a statistically steady flow is, following Townsend (1976), based on a local analysis of turbulence dynamics: quasi-isotropic turbulence is considered to be (i) generated by the breakdown of previously distorted eddies, then (ii) transported and distorted on a short enough time scale. (iii) Later nonlinear distortion and eddy breakdown occurs. RDT is aimed at explaining what happens to the eddies during (ii). In a steady state, all three stages are taking place simultaneously, but in many cases (ii) is significant enough to make RDT meaningful. Interestingly, it appears that the main effect of the nonlinearity is to impose a value on β. Maxey (1982) gives an upper bound equal to 3.5 for this effective shear and a closure equation for its computation. A further evaluation of order of magnitude confirms this experimental finding: in an equilibrium log layer, $S \approx u_\star/(k_0 z)$, and $t = t_e$, the eddy turnover time, where $t_e = \ell_e/u_e \approx (k_0 z)/u_\star \Rightarrow \beta = O(1)$ ℓ_e being the characteristic size of the eddies, u_e their characteristic fluctuation velocity, k_0 the Kármán constant and $u_\star$ the friction velocity. This result is consistent with Maxey's value.

Using inhomogeneous RDT (see Hunt & Graham (1978) for flows with no shear, and Lee & Hunt (1989) and Mann (1994) for sheared turbulence), estimates of all integral scales can be computed. In the present paper, we concentrate on the length scales based on the vertical velocity u_3 because this is the component mainly affected by blocking. Starting from the Navier–Stokes equations (2.1), neglecting the nonlinear term, taking the curl of the momentum equation and then the curl of the resulting equation, using the incompressibility condition to simplify the expressions, one obtains the equation for u_3:

$$(\partial_t + Sz\partial_3)\cdot(\Delta u_3) = 0, \tag{2.2}$$

where $\Delta = \nabla^2 = \partial^2/\partial x^2 + \partial^2/\partial y^2 + \partial^2/\partial z^2$. This equation is parabolic and therefore time appears explicitly in the solution. It is customary to use $\beta = St$ and to write $m_1 = k_1$, $m_2 = k_2$, $m_3 = k_3 - \beta k_1$, $k = (k_1^2 + k_2^2 + k_3^2)^{1/2}$, $m = (m_1^2 + m_2^2 + m_3^2)^{1/2}$ and $\kappa = (k_1^2 + k_2^2)^{1/2}$. With this notation, one can integrate (2.2) to give the two-dimensional Fourier transform $\tilde{u}_3(k_1, k_2, z, t)$ of the vertical velocity field:

$$\tilde{u}_3(k_1, k_2, z, t) = \frac{1}{2\pi}\int \frac{k^2}{m^2}\widehat{u}_3^H(k_1, k_2, k_3)(\mathrm{e}^{-\mathrm{i}m_3 z} - \mathrm{e}^{-\kappa z})\,\mathrm{d}k_3. \tag{2.3}$$

In the above equation, the first term in the parentheses on the right-hand side accounts for the shear effect, while the second one accounts for blocking (Mann 1994).

2.2. *Calculation of the integral scales*

Using the results of the above subsection, the general expressions for the integral scales according to RDT are now derived, starting with $L_{33}^{(y)}$, which is the simpler. As

seen in § 1,

$$L_{33}^{(y)} = \frac{\displaystyle\int_0^\infty \overline{u_3(\boldsymbol{x})u_3(\boldsymbol{x}+r\boldsymbol{e}_2)}\,\mathrm{d}r}{\overline{u_3^2}}.$$

Using some algebra, (2.3) leads to the following expression for the denominator of the definition of $L_{33}^{(y)}$:

$$\overline{u_3^2} = \frac{1}{(2\pi)^2}\iiint \Psi_{33}(k_1,k_2,k_3)|\mathrm{e}^{-\mathrm{i}m_3 z} - \mathrm{e}^{-\kappa z}|^2\,\mathrm{d}k_1\,\mathrm{d}k_2\,\mathrm{d}k_3 \tag{2.4}$$

where

$$\Psi(k_1,k_2,k_3) = \left[\frac{k_1^2+k_2^2+k_3^2}{k_1^2+k_2^2+(k_3-\beta k_1)^2}\right]^2 \Phi_{33}^H(k_1,k_2,k_3), \tag{2.5}$$

and Φ_{ij}^H is the correlation spectrum of initial homogeneous turbulence (e.g. Batchelor 1953).

For the numerator, we have to take the integral for r from 0 to ∞. The integral has the form $\int_0^\infty \mathrm{d}r \times \int_{-\infty}^\infty f(k_2)\mathrm{e}^{\mathrm{i}k_2 r}\,\mathrm{d}k_2$. But

$$\int_0^A \mathrm{d}r \times \int_{-\infty}^\infty f(k_2)\mathrm{e}^{\mathrm{i}k_2 r}\,\mathrm{d}k_2 = 2\int_0^\infty f(k_2)\frac{\sin k_2 A}{k_2}\,\mathrm{d}k_2$$

because f is even. Using lemma 1 in Appendix A to take the limit $A\to\infty$ leads to

$$\int_0^\infty \overline{u_3(x,y,z)u_3(x,y+r,z)}\,\mathrm{d}r = \frac{1}{(2\pi)^2}\frac{\pi}{2}\iint \Psi_{33}^H(m_1,0,m_3+\beta m_1)|\mathrm{e}^{-\mathrm{i}m_3 z} - \mathrm{e}^{-|m_1|z}|^2\,\mathrm{d}m_1\,\mathrm{d}m_3. \tag{2.6}$$

The complete expression for $L_{33}^{(y)}$ is given by the ratio of (2.4) and (2.6), which will be given for small z in § 2.3.

The calculation of $L_{33}^{(x)}$ is similar to that for $L_{33}^{(y)}$, and we get

$$\int_0^\infty \overline{u_3(x,y,z)u_3(x+r,y,z)}\,\mathrm{d}r = \frac{1}{(2\pi)^2}\frac{\pi}{2}\iint \Phi_{33}^H(0,k_2,k_3)\left|\mathrm{e}^{-\mathrm{i}k_3 z} - \mathrm{e}^{-|k_2|z}\right|^2\mathrm{d}k_2\,\mathrm{d}k_3. \tag{2.7}$$

Note that this expression is independent of the total shear β.

Similarly, one finds

$$\int_0^\infty \overline{u_3(x,y,z)u_3(x,y,z+r)}\,\mathrm{d}r = \int_0^\infty \mathrm{d}r \iiint \frac{k^4}{m^4}\Phi_{33}^H \times \left(\mathrm{e}^{-\mathrm{i}(k_3-\beta k_1)z} - \mathrm{e}^{-\kappa z}\right) \times \left(\mathrm{e}^{\mathrm{i}(k_3-\beta k_1)(z+r)} - \mathrm{e}^{-\kappa(z+r)}\right)\mathrm{d}k_1\,\mathrm{d}k_2\,\mathrm{d}k_3.$$

But now we cannot simply apply Lemma 1: we have to split the integral into parts for which we will be able to take the limit for $A\to\infty$ thanks to Lebesgue's lemma (lemma 2 in Appendix A), lemma 1 and the fact that $\int_0^\infty \mathrm{e}^{-\kappa r}\,\mathrm{d}r$ converges. After a few manipulations one obtains

$$\int_0^\infty \overline{u_3(x,y,z)u_3(x,y,z+r)}\,\mathrm{d}r = \frac{1}{(2\pi)^2}\frac{\pi}{2}\iint \Psi(m_1,m_2,0)(1-\mathrm{e}^{-\kappa z})\,\mathrm{d}m_1\,\mathrm{d}m_2 + \iiint \Psi(m_1,m_2,m_3)\left[\frac{\sin m_3 z}{m_3} - (\cos m_3 z - \mathrm{e}^{-\kappa z})\frac{\mathrm{e}^{-\kappa z}}{\kappa}\right]\mathrm{d}m_1\,\mathrm{d}m_2\,\mathrm{d}m_3. \tag{2.8}$$

Present notation	$\boldsymbol{m}$	z	q	$\boldsymbol{n}$	$\lvert\boldsymbol{m}\rvert^{\alpha}\Psi(\boldsymbol{m})$	K
Theorem notation	$\boldsymbol{x}$	l	j	$\boldsymbol{n}$	$f(\boldsymbol{x})$	K

TABLE 1. Notation correspondence for applying Theorems 1 and 2.

The calculation of $L_{33}^{(z-)}$ is similar, except for the finite limit of integration, which makes $\int_0^z \mathrm{e}^{\kappa r}\,\mathrm{d}r$ converge:

$$\int_0^z \overline{u_3(x,y,z)u_3(x,y,z-r)}\,\mathrm{d}r = \iiint \frac{k^4}{m^4}\Phi_{33}^H\,(\mathrm{e}^{-\mathrm{i}m_3 z}-\mathrm{e}^{-\kappa z}) \times\left[\frac{\mathrm{i}}{m_3}(1-\mathrm{e}^{\mathrm{i}m_3 z})-\frac{1}{\kappa}(1-\mathrm{e}^{-\kappa z})\right]\mathrm{d}k_1\,\mathrm{d}k_2\,\mathrm{d}k_3 \quad (2.9)$$

2.3. *Length scales for small z and a general spectrum*

Although the theory presented above is valid for any initial turbulent velocity field which extends in the whole space, we consider here an isotropic initial field for the sake of simplicity. Assume that the energy spectrum of this initial velocity field is $E(k)$, with integral scale L^H, and applies for $z \ll L^H$. In this section non-dimensional variables are used, writing z for z/L^H and $\boldsymbol{k}$ for $L^H\boldsymbol{k}$. It is known that for isotropic turbulence (e.g. Batchelor 1953),

$$\Phi_{ij}(\boldsymbol{k}) = \frac{E(|\boldsymbol{k}|)}{4\pi|k|^4}(|k|^2\delta_{ij}-k_i k_j).$$

Therefore, from (2.5),

$$\Psi(\boldsymbol{k}) = \frac{k_1^2+k_2^2}{4\pi\left(m_1^2+m_2^2+m_3^2\right)^2}E(k).$$

The 'potential' (Carlotti & Hunt 2003) energy spectrum is taken as a generalized Kármán spectrum of exponent $2p$,

$$E(k) = \frac{Ck^4}{(1+k^2)^{p+2}},$$

with $2p = q+\alpha$, k integer and $0<\alpha<1$ (C is a constant independent of k).

2.3.1. *Expansion of* $\overline{u_3^2}$

The following notation is used:

$$\overline{u_3^2} = \frac{1}{(2\pi)^2}J(z). \quad (2.10)$$

Writing $K(\boldsymbol{m}) = |\mathrm{e}^{-\mathrm{i}m_3} - \exp(-\sqrt{m_1^2+m_2^2})|^2$ and using the above notation and (2.4), we have $J(z) = \iiint \Psi(\boldsymbol{m})K(z\boldsymbol{m})\,\mathrm{d}\boldsymbol{m}$. Applying Theorem 1 (see Appendix B) in the case $\alpha \neq 0$ or Theorem 2 (see Appendix B) when $\alpha = 0$, we write $\boldsymbol{n} = \boldsymbol{m}/|\boldsymbol{m}|$ and the notation correspondence is given in table 1.

Using the following asymptotic behaviours:

$$|m|^{\alpha}\Psi(\boldsymbol{m}) = \underbrace{\frac{C}{4\pi}\frac{n_1^2+n_2^2}{\left[n_1^2+n_2^2+(n_3+\beta n_1)^2\right]^{q/2+\alpha/2}}}_{=f_{q+2}(\boldsymbol{n})}\frac{1}{|m|^{q+2}} + O\left(\frac{1}{|m|^{q+3}}\right), \qquad (2.11)$$

$$K(\boldsymbol{m}) = \underbrace{1}_{=K_2(\boldsymbol{n})} \times |m|^2 + O(|m|^3),$$

one finds

$$J(z) = az^{q-1+\alpha} + bz^2 + O(z^{q+\alpha}, z^3)$$

where

$$a = \mathrm{fp}\int_0^{\infty}\left[\iint K(r\boldsymbol{n})f_{q+2}(\boldsymbol{n})\,\mathrm{d}\boldsymbol{n}\right]\Big/ r^{q+\alpha}\mathrm{d}r,$$

$$b = \mathrm{fp}\int_0^{\infty}\left[\iint \Psi(r\boldsymbol{n})K_2(\boldsymbol{n})\,\mathrm{d}\boldsymbol{n}\right] r^{4-\alpha}\mathrm{d}r,$$

where fp $\int$ means that the integral should be understood in Hadamard's finite part sense (Carlotti 2001). Note that when $\alpha = 0$, Theorem 2 provides us with a logarithmic correction, but this term happens to vanish. Using some algebra:

$$\left.\begin{aligned} a &= \frac{C}{4\pi}\,\mathrm{fp}\int_0^{\infty}\left[\int_0^{2\pi}\int_0^{\pi}\frac{\left|\mathrm{e}^{-\mathrm{i}r\cos\theta} - \mathrm{e}^{-r|\sin\theta|}\right|^2\sin^2\theta}{[\sin^2\theta+(\cos\theta+\beta\sin\theta\cos\phi)^2]^p}\sin\theta\,\mathrm{d}\theta\,\mathrm{d}\phi\right]\frac{\mathrm{d}r}{r^{2p}},\\ b &= \frac{C}{4\pi}\mathrm{fp}\int_0^{\infty}\left[\int_0^{2\pi}\int_0^{\pi}\frac{\sin^2\theta[\sin^2\theta+(\cos\theta+\beta\sin\theta\cos\phi)^2]^2}{[1+r^2\sin^2\theta+r^2(\cos\theta+\beta\sin\theta\cos\phi)^2]^{p+2}}r^2\sin\theta\,\mathrm{d}\theta\,\mathrm{d}\phi\right]\frac{\mathrm{d}r}{r^{\alpha-4}}. \end{aligned}\right\} \qquad (2.12)$$

The only term in the Ψ expansion for which we have experimental or theoretical results is the first one. There is no reason to trust an expansion to a higher order. Therefore, depending on the value of $2p$:

$$\left.\begin{aligned} &1 < 2p < 3 : J(z) \sim az^{2p-1},\\ &3 < 2p < 4 : J(z) \sim bz^2. \end{aligned}\right\} \qquad (2.13)$$

2.3.2. *Expansion of* $L_{33}^{(x)}$

The same analysis as in § 2.3.1 is done here, with

$$I^x = (2\pi)^2\int_0^{\infty}\overline{u_3(x,y,z)u_3(x+r,y,z)}\,\mathrm{d}r.$$

From (2.7), we get $I^x = \pi/2\int\int\Psi(0,m_2,m_3)K(0,zm_2,zm_3)\,\mathrm{d}m_2\,\mathrm{d}m_3$. Therefore

$$I^x(z) = \pi/2[a^x z^{q+\alpha} + b^x z^2 + O(z^{q+1+\alpha}, z^3)]$$

with

$$a^x = \mathrm{fp}\int_0^{\infty}\left[\int K(r\boldsymbol{n}^x)f_{q+2}(\boldsymbol{n}^x)\,\mathrm{d}\boldsymbol{n}^x\right]\Big/ r^{q+\alpha+1}\,\mathrm{d}r,$$

$$b^x = \mathrm{fp}\int_0^{\infty}\left[\int \Psi(r\boldsymbol{n}^x)K_2(\boldsymbol{n}^x)\,\mathrm{d}\boldsymbol{n}^x\right] r^{3-\alpha}\,\mathrm{d}r,$$

where $\boldsymbol{n}^x = (0, n_2, n_3)$ represents the unity vector on the circle. Using some algebra:

$$\left.\begin{aligned} a^x &= \frac{C}{4\pi}\,\mathrm{fp}\int_0^\infty \left[\int_0^{2\pi} \left|\mathrm{e}^{-\mathrm{i}r\cos\theta} - \mathrm{e}^{-r|\sin\theta|}\right|^2 \sin^2\theta\,\mathrm{d}\theta\right]\frac{\mathrm{d}r}{r^{2p+1}}, \\ b^x &= \frac{C}{4\pi}\,\mathrm{fp}\int_0^\infty \left[\int_0^{2\pi} \frac{\sin^2\theta}{(1+r^2)^{p+2}} r^2 \mathrm{d}\theta\right]\frac{\mathrm{d}r}{r^{\alpha-3}}. \end{aligned}\right\} \tag{2.14}$$

For the same reason as for $J(z)$, the asymptotic expansion has to be truncated to a realistic order, giving

$$\left.\begin{aligned} &1 < 2p < 2 : I^x(z) \sim \frac{\pi}{2} a^x z^{2p}, \\ &2 < 2p < 4 : I^x(z) \sim \frac{\pi}{2} b^x z^2. \end{aligned}\right\} \tag{2.15}$$

Equations (2.13) and (2.15) lead to

$$\left.\begin{aligned} &1 < 2p < 2 : L_{33}^{(x)} \sim \frac{\pi}{2}\frac{a^x}{a} z, \\ &2 < 2p < 3 : L_{33}^{(x)} \sim \frac{\pi}{2}\frac{b^x}{a} z^{3-2p}, \\ &3 < 2p < 4 : L_{33}^{(x)} \sim \frac{\pi}{2}\frac{b^x}{b}. \end{aligned}\right\} \tag{2.16}$$

2.3.3. *Expansion of* $L_{33}^{(y)}$

The same analysis as in § 2.3.1 is done again, with

$$I^y = (2\pi)^2 \int_0^\infty \overline{u_3(x, y, z) u_3(x, y + r, z)}\,\mathrm{d}r.$$

From (2.6), we get $I^y = \pi/2 \int\int \Psi(m_1, 0, m_3) K(zm_1, 0, zm_3)\,\mathrm{d}m_1\,\mathrm{d}m_3$. Therefore

$$I^y(z) = \pi/2[a^y z^{q+\alpha} + b^y z^2 + O(z^{q+1+\alpha}, z^3)]$$

with

$$a^y = \mathrm{fp}\int_0^\infty \left[\int K(r\boldsymbol{n}^y) f_{q+2}(\boldsymbol{n}^y)\,\mathrm{d}\boldsymbol{n}^y\right] \Big/ r^{q+\alpha+1}\,\mathrm{d}r,$$

$$b^y = \mathrm{fp}\int_0^\infty \left[\int \Psi(r\boldsymbol{n}^y) K_2(\boldsymbol{n}^y)\,\mathrm{d}\boldsymbol{n}^y\right] r^{3-\alpha}\,\mathrm{d}r,$$

where $\boldsymbol{n}^y = (n_1, 0, n_3)$. Using some algebra:

$$\left.\begin{aligned} a^y &= \frac{C}{4\pi}\,\mathrm{fp}\int_0^\infty \left[\int_0^{2\pi} \frac{\left|\mathrm{e}^{-\mathrm{i}r\cos\theta} - \mathrm{e}^{-r|\sin\theta|}\right|^2 \sin^2\theta}{[\sin^2\theta + (\cos\theta + \beta\sin\theta)^2]^p}\,\mathrm{d}\theta\right]\frac{\mathrm{d}r}{r^{2p+1}}, \\ b^y &= \frac{C}{4\pi}\,\mathrm{fp}\int_0^\infty \left[\int_0^{2\pi} \frac{\sin^2\theta[\sin^2\theta + (\cos\theta + \beta\sin\theta)^2]^2}{[1 + r^2\sin^2\theta + r^2(\cos\theta + \beta\sin\theta)^2]^{p+2}} r^2\,\mathrm{d}\theta\right]\frac{\mathrm{d}r}{r^{\alpha-3}}. \end{aligned}\right\} \tag{2.17}$$

The truncation to the realistic order leads to

$$\left.\begin{aligned} &1 < 2p < 2 : I^y(z) \sim \frac{\pi}{2} a^y z^{2p}, \\ &2 < 2p < 4 : I^y(z) \sim \frac{\pi}{2} b^y z^2. \end{aligned}\right\} \tag{2.18}$$

Equations (2.13) and (2.18) lead to

$$\left.\begin{aligned} 1 < 2p < 2 &: L_{33}^{(y)} \sim \frac{\pi}{2}\frac{a^y}{a} z, \\ 2 < 2p < 3 &: L_{33}^{(y)} \sim \frac{\pi}{2}\frac{b^y}{a} z^{3-2p}, \\ 3 < 2p < 4 &: L_{33}^{(y)} \sim \frac{\pi}{2}\frac{b^y}{b}. \end{aligned}\right\} \tag{2.19}$$

2.3.4. *Expansion of* $L_{33}^{(z+)}$

Once more, the same analysis is done, with

$$I^{z+} = (2\pi)^2 \int_0^\infty \overline{u_3(x, y, z) u_3(x, y, z+r)}\, \mathrm{d}r.$$

From (2.8), we get

$$I^{z+} = \pi/2 \iint \Psi(m_1, m_2, 0)(1 - \mathrm{e}^{-\kappa z})\, \mathrm{d}m_1\, \mathrm{d}m_2$$
$$+ \iiint \frac{\Psi(m_1, m_2, m_3)}{\kappa} \left[\frac{\kappa \sin m_3 z}{m_3} - (\cos m_3 z - \mathrm{e}^{-\kappa z})\, \mathrm{e}^{-\kappa z}\right] \mathrm{d}m_1\, \mathrm{d}m_2\, \mathrm{d}m_3 (= I^{z1+} + I^{z2+}).$$

The following asymptotic expansions are needed:

$$1 - \mathrm{e}^{-\kappa} = \kappa - (1/2)\kappa^2 + (1/6)\kappa^3 + O(\kappa^4),$$

$$\frac{\kappa \sin m_3}{m_3} - (\cos m_3 - \mathrm{e}^{-\kappa})\, \mathrm{e}^{-\kappa} = \left(\frac{3}{2}\frac{\kappa^2}{|m|^2} + \frac{1}{2}\frac{m_3^2}{|m|^2}\right) |m|^2 + O(|m|^3).$$

This leads to

$$I^{z1+}(z) = \frac{\pi}{2}\left[a_1^{z+} z^{q+\alpha} + b_1^{z+} z + O(z^{q+1+\alpha}, z^2)\right],$$

$$I^{z2+}(z) = a_2^{z+} z^{q+\alpha} + b_2^{z+} z^2 + O(z^{q+1+\alpha}, z^2).$$

Truncating to realistic order, we have for $1 < 2p < 4$:

$$I^{z+}(z) \sim \frac{\pi}{2} b_1^{z+}. \tag{2.20}$$

Denoting $b^{z+} = b_1^{z+}$, (2.13) and (2.20) lead to

$$\left.\begin{aligned} 1 < 2p < 3 &: L_{33}^{(z+)} \sim \frac{\pi}{2}\frac{b^{z+}}{a} z^{2-2p}, \\ 3 < 2p < 4 &: L_{33}^{(z+)} \sim \frac{\pi}{2}\frac{b^{z+}}{b} z^{-1}, \end{aligned}\right\} \tag{2.21}$$

with

$$b^{z+} = \mathrm{fp} \int_0^\infty \left[\int \Psi(r\boldsymbol{n}^z) K_1(\boldsymbol{n}^z)\, \mathrm{d}\boldsymbol{n}^z\right] r^{2-\alpha}\, \mathrm{d}r$$

where $\boldsymbol{n}^z = (n_1, n_2, 0)$, $K(\boldsymbol{n}^z) = 1 - \exp(-\sqrt{n_1^2 + n_2^2})$ and therefore $K_1(\boldsymbol{n}^z) = 1$ from the asymptotic expansions derived above. Using some algebra,

$$b^{z+} = \frac{C}{4\pi}\, \mathrm{fp} \int_0^\infty \left[\int_0^{2\pi} \frac{r^2\left(1 + \beta^2 \cos^2\theta\right)}{\left(1 + r^2 + r^2\beta^2 \cos^2\theta\right)^{p+2}}\, \mathrm{d}\theta\right] \frac{\mathrm{d}r}{r^{\alpha-2}}. \tag{2.22}$$

2.3.5. *Expansion of* $L_{33}^{(z-)}$

Now $I^{z-}=(2\pi)^2\int_0^z \overline{u_3(x,y,z-r)u_3(x,y,z)}\,\mathrm{d}r$ is considered. From (2.9), we can write $I^{z-}=\iiint |m|^{-1}\Psi(k_1,k_2,k_3)K(z\boldsymbol{k})\,\mathrm{d}k_1\,\mathrm{d}k_2\,\mathrm{d}k_3$ with the following correspondence relationships:

$$|\boldsymbol{m}|^{\alpha-1}\Psi(\boldsymbol{m}) \qquad \leftrightarrow f(\boldsymbol{x}),$$

$$(\mathrm{e}^{-\mathrm{i}m_3}-\mathrm{e}^{-\kappa})\left[\frac{\mathrm{i}m}{m_3}(1-\mathrm{e}^{\mathrm{i}m_3})-\frac{m}{\kappa}(1-\mathrm{e}^{-\kappa})\right]\leftrightarrow K(\boldsymbol{m}),$$

so from (2.12), $f_{q+2}(\boldsymbol{n})$ becomes $f_{q+3}(\boldsymbol{n})$ and using some algebra, one can show that

$$K(\boldsymbol{m})=\underbrace{1/2}_{=K_2(\boldsymbol{n})}\times|m|^2+O(|m|^3). \tag{2.23}$$

Therefore

$$I^{z-}=a^{z-}z^{2p}+b^{z-}z^2+c^{z-}z^3+O(z^{2p+1},z^4).$$

The evaluation of b^{z-} shows that it is zero, and therefore, truncated to the realistic order,

$$\left.\begin{array}{ll} 1<2p<3: & I^{z-}\sim a^{z-}z^{2p},\\ 3<2p<4: & I^{z-}\sim c^{z-}z^3,\end{array}\right\} \tag{2.24}$$

with

$$a^{z-}=\mathrm{fp}\int_0^\infty\left[\int K(r\boldsymbol{n})f_{q+3}(\boldsymbol{n})\,\mathrm{d}\boldsymbol{n}\right]\Big/ r^{q+\alpha+1}\,\mathrm{d}r,$$

$$c^{z-}=\mathrm{fp}\int_0^\infty\left[\int \Psi(r\boldsymbol{n})K_2(\boldsymbol{n})\,\mathrm{d}\boldsymbol{n}\right] r^{4-\alpha}\,\mathrm{d}r,$$

which leads to

$$\left.\begin{array}{l} a^{z-}=\dfrac{C}{4\pi}\,\mathrm{fp}\displaystyle\int_0^\infty\left[\int_0^{2\pi}\int_0^{\pi}\frac{\left(\mathrm{e}^{-\mathrm{i}r\cos\theta}-\mathrm{e}^{-r|\sin\theta|}\right)\left[\frac{i(1-\mathrm{e}^{-\mathrm{i}r\cos\theta})}{\cos\theta}-\frac{1-\mathrm{e}^{-r|\sin\theta|}}{|\sin\theta|}\right]\sin^2\theta}{[\sin^2\theta+(\cos\theta+\beta\sin\theta\cos\phi)^2]^p}\sin\theta\,\mathrm{d}\theta\,\mathrm{d}\phi\right]\frac{\mathrm{d}r}{r^{2p}},\\ c^{z-}=\dfrac{C}{4\pi}\,\mathrm{fp}\displaystyle\int_0^\infty\left[\int_0^{2\pi}\int_0^{\pi}\frac{1}{2}\frac{\sin^2\theta[\sin^2\theta+(\cos\theta+\beta\sin\theta\cos\phi)^2]^2}{[1+r^2\sin^2\theta+r^2(\cos\theta+\beta\sin\theta\cos\phi)^2]^{p+2}}r\sin\theta\,\mathrm{d}\theta\,\mathrm{d}\phi\right]\frac{\mathrm{d}r}{r^{\alpha-4}},\end{array}\right\} \tag{2.25}$$

Using, (2.13) and (2.24), we have

$$\left.\begin{array}{ll} 1<2p<3: & L_{33}^{(z-)}\sim\dfrac{\pi}{2}\dfrac{a^{z-}}{a}z,\\ 3<2p<4: & L_{33}^{(z-)}\sim\dfrac{\pi}{2}\dfrac{c^{z-}}{b}z.\end{array}\right\} \tag{2.26}$$

3. High-resolution LES of the neutral atmospheric boundary layer

3.1. *The LES model*

The large-eddy simulations presented in this paper were made using Méso-NH, an LES and meso-scale code developed by CNRM (Météo France and CNRS) and Laboratoire d'Aérologie (CNRS) (Lafore *et al.* 1998). In this paper, it is used

exclusively in its LES mode. Méso-NH is designed to be a general purpose atmospheric code, and can therefore deal with stable and unstable conditions, and accommodate moisture and vapour content computations. All these modules are switched off in the present simulations, and therefore, in the following only the equations simplified for the neutral case are presented.

The principle of any large-eddy simulation is to compute a spatially filtered version of the actual velocity field. Here, we denote by a tilde the filtering operation. Starting with the Navier–Stokes equations, assuming that the filtering operation commutes with differentiation, which is true as a first approximation, the equation for the filtered velocity field is obtained:

$$\left.\begin{aligned} &\partial_t \widetilde{u_i} + \partial_j \widetilde{u_i}\widetilde{u_j} = -\partial_i \widetilde{p} - \partial_j \Gamma(u_i, u_j) + \nu \Delta \widetilde{u_i} + 2(\boldsymbol{\Omega} \times \widetilde{\boldsymbol{u}})_i, \\ &\partial_i \widetilde{u_i} = 0, \end{aligned}\right\} \tag{3.1}$$

where ν is the kinematic viscosity and $\Gamma(f, g) = \widetilde{fg} - \widetilde{f}\widetilde{g}$. In all the atmospheric calculations, the viscous term $\nu \Delta \widetilde{u_i}$ is very small compared with the subgrid stresses $\partial_j \Gamma(u_i, u_j)$ and is therefore neglected. The term $2\boldsymbol{\Omega} \times \widetilde{\boldsymbol{u}}$ represents the forcing of the flow by Coriolis forces. The equations (3.1) do not constitute a closed system, since the subgrid stresses depend on the unfiltered velocity field. Some extra modelling is required in order to close these equations. In Méso-NH this is done using the subgrid kinetic energy (Cuxart, Bougeault & Redelsperger 2000):

$$e = \tfrac{1}{2}(\Gamma(u_1, u_1) + \Gamma(u_2, u_2) + \Gamma(u_3, u_3)) \tag{3.2}$$

as a prognostic variable, i.e. by writing an empirical evolution equation for e and an equation relating e and $\Gamma(u_i, u_j)$:

$$\partial_t e = -\partial_k(\widetilde{u_k} e) - \Gamma(u_i, u_k)\partial_k \widetilde{u_i} - \partial_j(C_{2m} L \sqrt{e} \partial_j e) - \varepsilon, \tag{3.3a}$$

$$\varepsilon = C_\varepsilon \frac{e^{3/2}}{L}, \tag{3.3b}$$

$$\Gamma(u_i, u_j) = \frac{2}{3}\delta_{ij} e - \frac{4}{15}\frac{L}{C_m}\sqrt{e}\left(\partial_j \widetilde{u_i} + \partial_i \widetilde{u_j} - \tfrac{2}{3}\delta_{ij}\partial_k \widetilde{u_k}\right). \tag{3.3c}$$

In the above set of equations, C_m, C_{2m} and C_ε are non-dimensional constants and L is a length scale. Consideration of the free-stream turbulence properties (in particular the assumption that turbulence has a Kolmogorov $k^{-5/3}$ power spectrum) suggests using $C_m = 4$, $C_{2m} = 0.2$, $C_\varepsilon = 0.7$ and $L = (\Delta x \Delta y \Delta z)^{1/3}$ where Δx, Δy, and Δz are the mesh sizes (Schmidt & Schumann 1989).

The set of equations (3.1) and (3.3) is closed provided boundary conditions are given. In the present simulations, the flow domain is assumed to be periodic in the horizontal directions, so that the lateral boundary conditions are set by periodicity. At the top a rigid lid is placed, i.e.

$$\left.\begin{aligned} \widetilde{u_3} &= 0, \\ \Gamma(u_i, u_j) &= 0. \end{aligned}\right\} \tag{3.4}$$

Therefore $e = 0$ at the top of the flow domain. The horizontal velocities at the top of the domain are given by the geostrophic forcing.

The boundary condition at the ground is calculated using the assumption that the velocity field of the large eddies $\widetilde{u_i}$ below the first grid point behaves like the mean flow of a boundary layer, i.e. that an instantaneous log-law is valid close to the wall

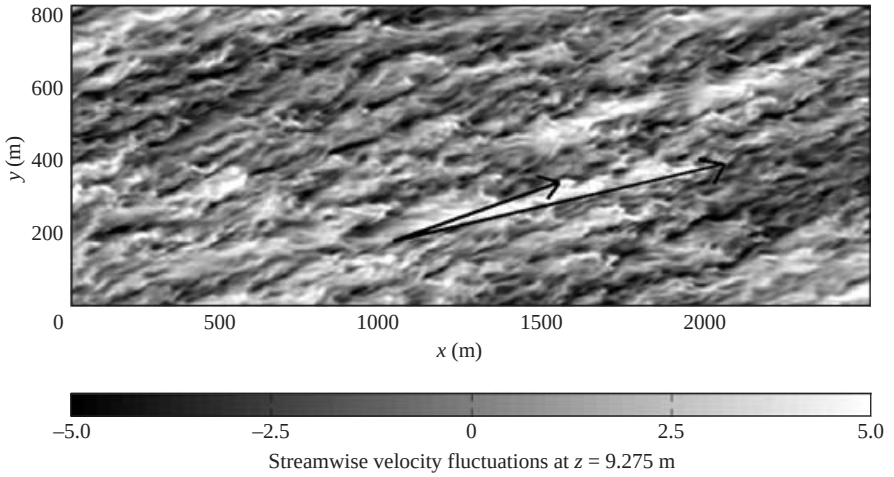

FIGURE 4. Snapshot of the turbulent longitudinal (or streamwise) velocity close to the ground ($z \simeq 10$ m), normalized by the friction velocity u_*. The snapshot shows evidence of elongated streaks of 300 m average spacing. The shorter arrow indicates the surface wind vector ($\simeq 5\,\mathrm{m\,s^{-1}}$) and the longer arrow the upper-level wind vector ($\simeq 10\,\mathrm{m\,s^{-1}}$) (which is nearly geostrophic).

(Schmidt & Schumann 1989):

$$\Gamma(u_1, u_3) = -\frac{\widetilde{u}_1}{\widetilde{u}} u_*^2, \tag{3.5a}$$

$$\Gamma(u_2, u_3) = -\frac{\widetilde{u}_2}{\widetilde{u}} u_*^2, \tag{3.5b}$$

$$u_* = k_0 \widetilde{u} / \ln \frac{x_3}{z_0}, \tag{3.5c}$$

where $\widetilde{u} = \sqrt{\widetilde{u_1}^2 + \widetilde{u_2}^2}$ is the filtered streamwise velocity and $u_*(x_1, x_2, t)$ is to be determined. In the present simulation, the roughness length z_0 is imposed and u_* is computed by applying (3.5*c*) in the first cell close to the ground, i.e. at the height $\Delta z/2$. The subgrid kinetic energy e in that cell is calculated using (3.3*a*), where the term $\Gamma(u_i, u_k)\partial_k \widetilde{u_i}$ is interpolated from its value at $x_3 = \Delta z + \Delta z/2$. The mean velocity is computed from (3.1) and (3.5). This boundary condition is a crucial feature of the model, because it is impossible to resolve the viscous sublayer, which is only a few millimetres thick.

3.2. *Streamwise large eddies, spectra and integral length scales*

A neutrally stratified, mid-latitude, barotropic and dry ABL was simulated on a domain 3 km long, 1 km wide and 750 m high (figure 4). The computational grid is cubic to avoid any influence of anisotropy of the grid, with a 6.25 m mesh (Carlotti 2002). The simulation domain is assumed to be placed at 45° North, and for the forcing we assume a large-scale pressure gradient that would balance a geostrophic wind of $U_1 = 10\ \mathrm{m\,s^{-1}}$ above the boundary layer. The friction velocity found in the LES is $u_\star = 0.4\ \mathrm{m\ s^{-1}}$.

The fine-scale structures found near the ground are shown in figure 4. These organized large eddies in the form of near-surface streaks are ubiquitous features of LES of the ABL in which shear plays an important role in the dynamics (Deardorff 1972; Moeng & Sullivan 1994; Lin *et al.* 1996; Drobinski & Foster 2003). Streaks reside within the high-shear surface region (i.e. the surface layer and the lower ABL).

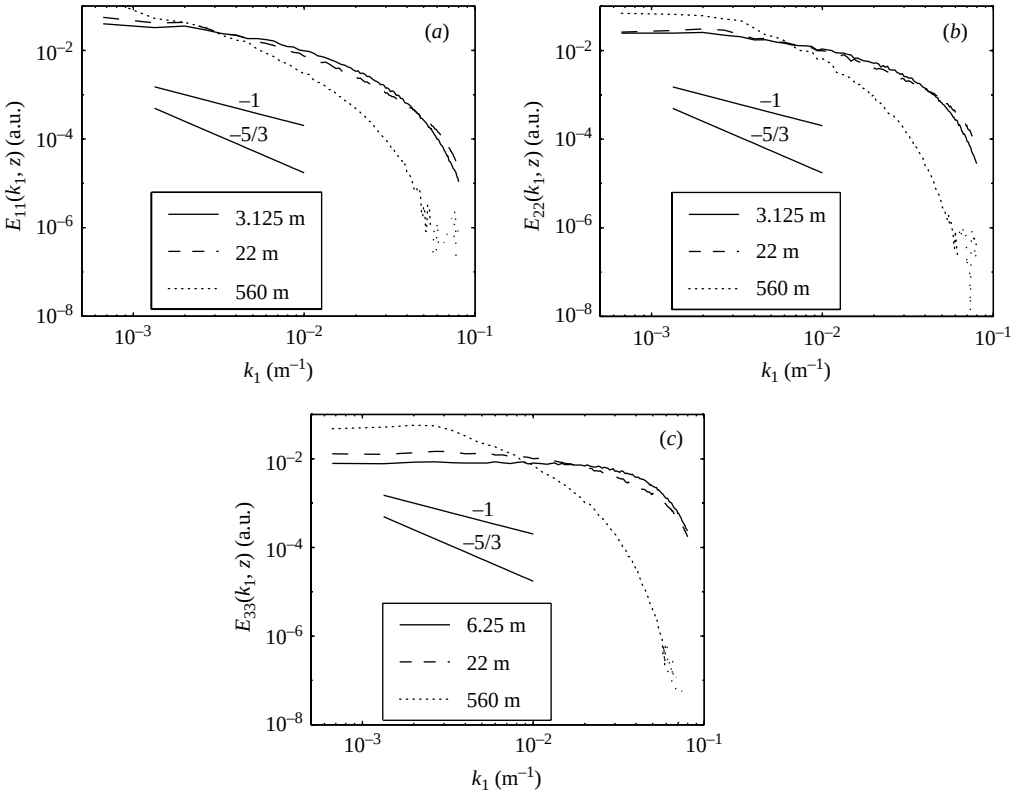

FIGURE 5. Longitudinal (or streamwise) (*a*), transverse (*b*) and vertical (*c*) velocity fluctuation spectra computed from the LES velocity field. The solid, dashed and dotted lines correspond to the first staggered grid level (i.e. 3.125 m for E_{11} and E_{22} and 6.25 m for E_{33}) and to approximately 22 and 560 m, respectively. The two segments show the $-5/3$ and -1 slopes (the value of the slope is indicated).

As shown in figure 4, they are best visualized in cross-sections parallel to the surface that show organized regions of alternating high- and low-speed fluid for any one of the three velocity components. In figure 4, the streak spacing is about 300 m and they have a 100 m vertical extent. Streaks form, evolve and decay over relatively short lifetimes of several tens of minutes after which they rapidly regenerate (Foster 1997; Drobinski & Foster 2003; Drobinski *et al.* 2004). Near-surface streaks have been found experimentally in a near-neutral atmospheric surface layer (Weckwerth, Grund & Mayor 1997; Drobinski *et al.* 2004).

Longitudinal spectra at several heights are shown in figure 5. They show a clear trend towards a k_1^{-1} slope at intermediate wavenumbers when the height decreases, in accordance with atmospheric experimental evidence (Drobinski *et al.* 2004). Indeed, figure 5 shows evidence of the two sublayers of the surface layer: very close to the ground, a k_1^{-1} subrange is visible on the longitudinal and transverse velocity fluctuation spectra only (eddy surface layer); at 22 m, a k_1^{-1} subrange is found in the spectra of the three velocity fluctuation components and at 560 m, the turbulence displays isotropic characteristics. More precisely, the LES gives access to the depths of the eddy and shear surface layers which are about 20 and 270 m, respectively. Because of the limited resolution of the LES, because of the subgrid model, effect of

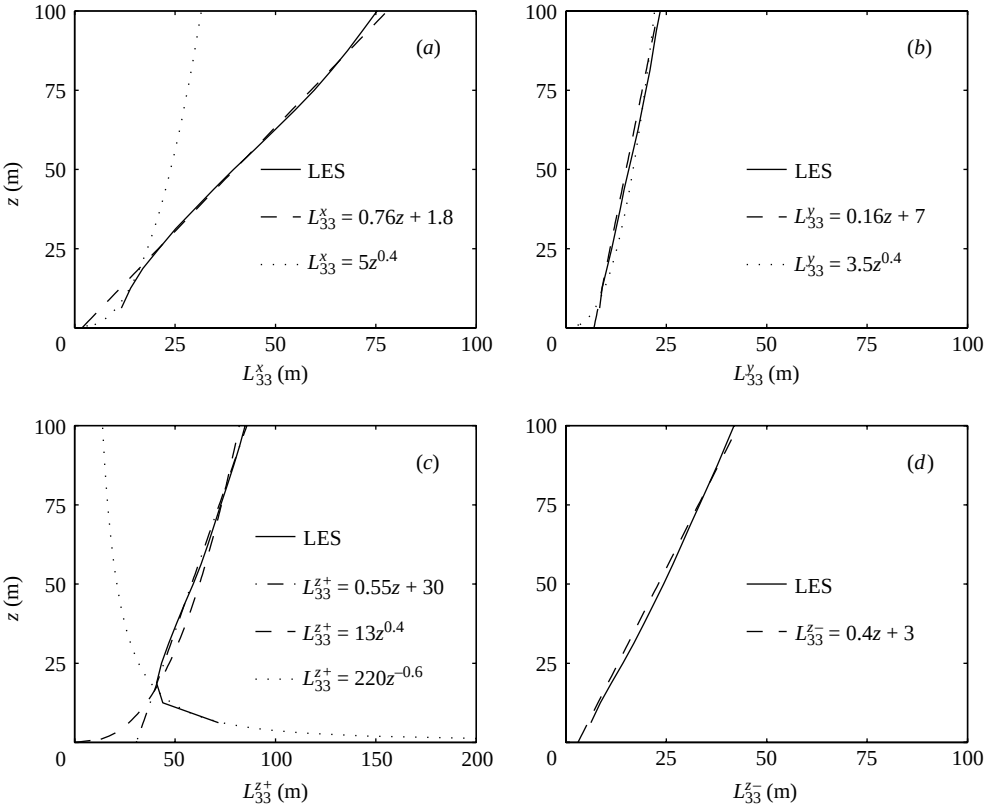

FIGURE 6. Integral scales L_{33}^{x} (*a*), L_{33}^{y} (*b*), L_{33}^{z+} (*c*) and L_{33}^{z-} (*d*) computed from the LES velocity field (solid line). The dashed, dotted and dash-dotted curves correspond to different approximations of the integral length scales in the region below or above the third grid point, as indicated.

which is felt at wavenumbers smaller than the cut-off wavenumber, and because of numerical diffusion, spectra are significantly damped for large wavenumbers. Close to the ground, the Kolmogorov range does not exist, and the k_1^{-1} subrange is itself damped, since the filtering length (6.25 m) is of the same order as the height and the large-scale limit of the Kolmogorov range should be also of the same order (Kaimal *et al.* 1972; Hunt & Carlotti 2001; Högström, Hunt & Smedman 2002; Drobinski *et al.* 2004).

Figure 6 displays the vertical profiles of the integral length scales $L_{33}^{x_i\pm}$ computed from the simulated velocity field using (1.1) and (1.2). Above the third grid point, the vertical profiles of $L_{33}^{x_i\pm}$ have a linear or quasi-linear shape, whereas close to the ground, the vertical profiles of L_{33}^{z+}, in particular, decrease as $z^{-0.6}$ with z.

4. Behaviour of the integral scales

4.1. *Not all length scales are proportional to z*

Defining γ_i by the following equations:

$$L_{33}^{(x)} \propto z^{\gamma_1}, \quad L_{33}^{(y)} \propto z^{\gamma_2}, \quad L_{33}^{(z+)} \propto z^{\gamma_3}, \quad L_{33}^{(z-)} \propto z^{\gamma_4},$$

$1 < 2p < 2$: slow roll-off (typical of high-Reynolds-number turbulence)	$2 < 2p < 3$	$3 < 2p < 4$: fast roll-off (typical of low-Reynolds-number turbulence or turbulence calculated with subgrid models)
	$\rightarrow$	
$\gamma_1 = 1$	$0 < \gamma_1 = 3 - 2p < 1$	$\gamma_1 = 0$
$\gamma_2 = 1$	$0 < \gamma_2 = 3 - 2p < 1$	$\gamma_2 = 0$
$0 < \gamma_3 = 2 - 2p < 1$	$-1 < \gamma_3 = 2 - 2p < 0$	$\gamma_3 = -1$
$\gamma_4 = 1$	$\gamma_4 = 1$	$\gamma_4 = 1$

TABLE 2. Asymptotic behaviour of integral scales, from (2.16), (2.19), (2.21) and (2.26).

	$L_{33}^{(x)}$	$L_{33}^{(y)}$	$L_{33}^{(z+)}$	$L_{33}^{(z-)}$
$1 < 2p < 2$	$\frac{\pi}{2}\frac{a^x}{a}z$	$\frac{\pi}{2}\frac{a^y}{a}z$	$\frac{\pi}{2}\frac{b^{z+}}{a}z^{2-2p}L_H^{2p-1}$	$\frac{a^{z-}}{a}z$
$2 < 2p < 3$	$\frac{\pi}{2}\frac{b^x}{a}z^{3-2p}L_H^{2p-2}$	$\frac{\pi}{2}\frac{b^y}{a}z^{3-2p}L_H^{2p-2}$	$\frac{\pi}{2}\frac{b^{z+}}{a}z^{2-2p}L_H^{2p-1}$	$\frac{a^{z-}}{a}z$
$3 < 2p < 4$	$\frac{\pi}{2}\frac{b^x}{b}L_H$	$\frac{\pi}{2}\frac{b^y}{b}L_H$	$\frac{\pi}{2}\frac{b^{z+}}{b}z^{-1}L_H^2$	$\frac{b_3^{z-}}{b}z$

TABLE 3. Dimensional expressions for $L_{33}^{(x)}$, $L_{33}^{(y)}$, $L_{33}^{(z+)}$ and $L_{33}^{(z-)}$.

and using (2.16), (2.19), (2.21) and (2.26), the results can be summarized in table 2. Note that they are valid in the general shear plus blocking case (the values of the constant being determined by the shear from (2.12), (2.14), (2.17), (2.22) and (2.25)).

Table 2 shows that if all the eddy scales are proportional to z, then $2p \rightarrow 1$. As a corollary, if the spectral exponent $2p \neq 1$, the eddy length scales are not proportional to z and therefore are inconsistent with a naive dimensional analysis formulation of the equilibrium log-layer theory. This shows that scaling assumptions are not unique and that they are closely related to the form of spectra. Indeed, the reason why the simple dimensional argument (according to which the distance to the boundary is the only autonomous length scale) does not apply is that, because of the top-down characteristic of the the surface layer, a second length scale appears in our problem, namely the integral scale of turbulence far away from the boundary L^H. Hence dimensional analysis gives

$$L = L^H \phi(z/L^H)$$

where L is one of the integral lengths. From this dimensional analysis, it is not possible to determine the function ϕ. The above RDT calculation offers a way of calculating ϕ. Because in the above calculation all the length were determined with respect to L^H, the dimensional version of (2.16), (2.19), (2.21) and (2.26) is given in table 3.

Table 2 allows the vertical profiles of the length scales obtained from the LES velocity field to be interpreted, as shown in figure 6. One can see very clearly that $\gamma_4 = 1$ with a very good agreement. For $z \geqslant 20$ m, the results of table 2 for $L_{33}^{(x)}$, $L_{33}^{(y)}$ and $L_{33}^{(z-)}$ are reproduced well with $\gamma_1 = \gamma_2 = \gamma_4 = 1$. For $L_{33}^{(z+)}$, two approximate curves are plotted corresponding to $\gamma_4 = 0.4$ (i.e. $2p = 1.6 \approx 5/3$) (dashed line) and $\gamma_4 = 1$ (i.e. $2p = 1$) (dash-dotted line). The linear fit $0.55z + 30$ corresponds to a spectral subrange with a -1 power law when the constant 30 is smaller than the $0.55z$ term. This implies the existence of the spectral subrange with a -1 power law for z large enough. This is in good agreement with the LES spectra (see figure 5)

	$2p = 5/3$	$2p = 1.5$	$2p = 1.3$	$2p = 1.1$	$2p = 1.01$
$\beta = 0$	$k_0 = 0.47$	$k_0 = 0.42$	$k_0 = 0.33$	$k_0 = 0.22$	$k_0 = 0.20$
$\beta = 2$	$k_0 = 0.45$	$k_0 = 0.40$	$k_0 = 0.31$	$k_0 = 0.21$	$k_0 = 0.19$
$\beta = 4$	$k_0 = 0.45$	$k_0 = 0.39$	$k_0 = 0.31$	$k_0 = 0.21$	$k_0 = 0.19$
$\beta \to \infty$	$k_0 \to 0.45$	$k_0 \to 0.39$	$k_0 \to 0.31$	$k_0 \to 0.21$	$k_0 \to 0.19$

TABLE 4. Values of k_0 computed numerically for various values of $2p$.

and the experimental results obtained by Drobinski *et al.* (2004) in the shear surface layer. However, for $z \leqslant 20$ m, $L_{33}^{(z+)}$ increases with decreasing z. Assuming a spectrum decay $2p = 2.6$, this corresponds very well with the values predicted by RDT. This corresponds to the fast decay of the spectrum due to subgrid model (figure 5).

4.2. *Consequence for the mixing length*

The basic argument of classical boundary layer theory is that, from dimensional analysis (see Prandtl 1952), the mixing length, which is the length scale related to Reynolds stress, should be proportional to the distance to the wall, $\ell_m = k_0 z$, where k_0 is the Kármán constant. Using his conical eddy hypothesis, Townsend (1976), assuming as a starting point that the mixing length ℓ_m is proportional to z, was able to derive the value of Kármán constant $k_0 \approx 0.32$, the a value which depends on the actual shape of the eddies. Malkus (1956), using arguments of stability theory was able to find $k_0 \approx 0.33$.

The physical interpretation of the mixing length as the vertical length on which, on average, the velocity fields are de-correlated makes it clear that it should be very close to the smaller vertical integral scales of the flow, as Prandtl (1952) noticed. Therefore, one must have

$$\ell_m \sim L_{33}^{(z-)}. \tag{4.1}$$

From table 3, $L_{33}^{(z-)} = (a^{z-}/a)z$. Thus, our analysis shows that

$$\ell_m \sim k_0 z,$$

where k_0 depends *a priori* on β and is given by $k_0 = a^{z-}/a$, a^{z-} and a being given by (2.25). From this theory, k_0 can be computed numerically for several values of the spectrum decay rate, between $2p = 5/3$ and $2p = 1$ (table 4).

Note that k_0 depends only very weakly on β. This indicates that RDT is performing well in the present case, even though it assumes a constant shear whereas in a logarithmic layer the shear is not constant. The computed values for $2p = 5/3$ show a good agreement with the experimental value of 0.4. In the ESL, one should expect a value of k_0 between the two extremes, i.e. 0.5 and 0.2, as the form of the spectrum displays both a -1 and $-5/3$ spectral range.

5. Elongated large eddies

Near-surface elongated large eddies (figure 4) are generated near the ground and carry most of the turbulent fluxes of momentum (and buoyancy in the ABL) (e.g. Mahrt & Gibson 1992; Högström & Bergström 1996; Lin *et al.* 1996) and are of crucial importance for energy balance issues and for LES that have to represent at least the strongest of these structures.

In order to study these large eddies, one can use the ratios $L_{ij}^{(x)}/L_{kl}^{(y)}$ with i, j, k, and l suitably chosen. Elongated large eddies from pure shear RDT were shown

in Hunt & Carruthers (1990) by visualization of the distorted u_1 and u_2 fields. It was decided in the present work to focus on the the effect of blocking on the vertical velocity, comparing the pure shear and the shear plus blocking cases. For this purpose, the ratio $L_{33}^{(x)}/L_{33}^{(y)}$ is a good indicator of the effect of turbulence distortion in the presence of shear or/and a wall. The influence of the non-dimensional shear β and the spectrum decay rate $2p$ will also be investigated.

5.1. *Shear with blocking* (*near-wall turbulence*)

From table 3, the ratio $L_{33}^{(x)}/L_{33}^{(y)}$ for $1 < 2p < 2$ is given by

$$\frac{L_{33}^{(x)}}{L_{33}^{(y)}} = \frac{a^x}{a^y}. \tag{5.1}$$

From (2.14), a^x is independent of β:

$$a^x = 4C/4\pi \int_0^{\pi/2} F(2p+1,\theta)\sin^2\theta\,\mathrm{d}\theta$$

where

$$F(q,\theta) = \int_0^\infty \frac{\left|\mathrm{e}^{-\mathrm{i}r\cos\theta} - \mathrm{e}^{-r|\sin\theta|}\right|^2}{r^q}\,\mathrm{d}r$$
$$= \int_0^\infty \frac{\left(\cos(r\cos\theta) - \mathrm{e}^{-r|\sin\theta|}\right)^2 + \sin^2(r\cos\theta)}{r^q}\,\mathrm{d}r.$$

For small β ($0 \leqslant \beta \leqslant 10$), the expression for a^y in (2.17) can be expanded quite easily using classical techniques, leading to

$$a^y = \frac{4C}{4\pi}\left\{\int_0^{\pi/2} F(2p+1,\theta)\sin^2\theta\,\mathrm{d}\theta + p[(2p+1)\int_0^{\pi/2} F(2p+1,\theta)\sin^4\theta\,\mathrm{d}\theta\right.$$
$$\left. -(2p+2)\int_0^{\pi/2} F(2p+1,\theta)\sin^6\theta\,\mathrm{d}\theta]\beta^2 + O(\beta^3)\right\}.$$

The values of $L_{33}^{(x)}/L_{33}^{(y)}$ can be directly computed for finite β using (2.16) and (2.19).

From table 3, the ratio $L_{33}^{(x)}/L_{33}^{(y)}$ for $2 < 2p < 3$ and $3 < 2p < 4$ is given by

$$\frac{L_{33}^{(x)}}{L_{33}^{(y)}} = \frac{b^x}{b^y}. \tag{5.2}$$

For $2 < 2p < 3$, $\alpha = 2p - 2$ and for $3 < 2p < 4$, $\alpha = 2p - 3$. Equation (2.14) gives

$$b^x = \begin{cases} \dfrac{4C}{4\pi}\,\dfrac{\pi}{4}\displaystyle\int_0^\infty \frac{r^{7-2p}}{(1+r^2)^{p+2}}\,\mathrm{d}r & \text{for} \quad 2 < 2p < 3 \\ \dfrac{4C}{4\pi}\,\dfrac{\pi}{4}\displaystyle\int_0^\infty \frac{r^{8-2p}}{(1+r^2)^{p+2}}\,\mathrm{d}r & \text{for} \quad 3 < 2p < 4, \end{cases}$$

which is independent of β. Equation (2.17) gives

$$b^y = \begin{cases} \dfrac{C}{4\pi}\displaystyle\int_0^\infty\int_0^{2\pi} \frac{r^{7-2p}\sin^2\theta[\sin^2\theta + (\cos\theta + \beta\sin\theta)^2]^2}{[1 + r^2\sin^2\theta + r^2(\cos\theta + \beta\sin\theta)^2]^{p+2}}\,\mathrm{d}r\,\mathrm{d}\theta & \text{for} \quad 2 < 2p < 3 \\ \dfrac{C}{4\pi}\displaystyle\int_0^\infty\int_0^{2\pi} \frac{r^{8-2p}\sin^2\theta[\sin^2\theta + (\cos\theta + \beta\sin\theta)^2]^2}{[1 + r^2\sin^2\theta + r^2(\cos\theta + \beta\sin\theta)^2]^{p+2}}\,\mathrm{d}r\,\mathrm{d}\theta & \text{for} \quad 3 < 2p < 4. \end{cases}$$

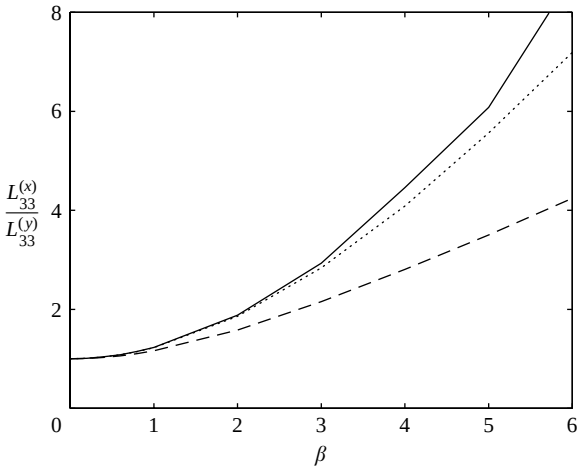

FIGURE 7. $L_{33}^{(x)}/L_{33}^{(y)}$ as a function of β for $2p = 5/3$ (solid line), $2p \to 1$ (dashed line) and $2p = 2.6$ (dotted line).

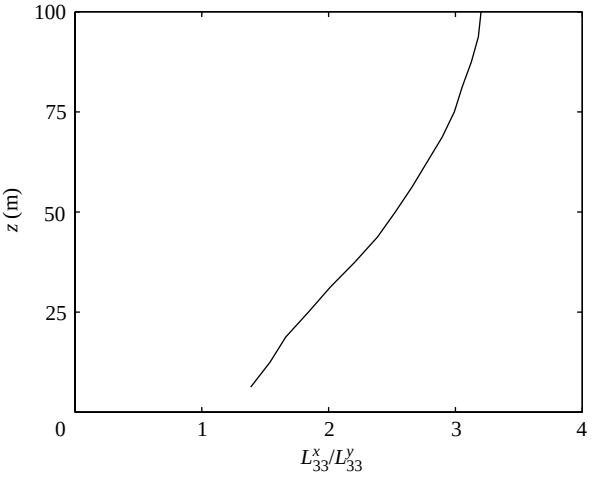

FIGURE 8. $L_{33}^{(x)}/L_{33}^{(y)}$ as a function of height, computed from the LES.

Figure 7 displays the value of $L_{33}^{(x)}/L_{33}^{(y)}$ as a function of β for $2p = 5/3$ (solid line), $2p \to 1$ (dashed line) and $2p = 2.6$ (dotted line). It can be used to analyse figure 8 which shows the ratio $L_{33}^{(x)}/L_{33}^{(y)}$ computed from LES results as a function of z. It can be seen that the ratio increases from 1.4 to 3 with height, which is reasonable aspect ratio for the streaky structures that can be observed in the real atmosphere or simulated in LES. Wilczak & Tillman (1980), using a network of *in-situ* temperature and velocity sensors, showed that under slightly unstable, high-wind-speed conditions, near-surface plumes are distinctly elongated in the mean wind direction with typical longitudinal and lateral dimensions of several hundred and several tens of metres, respectively. According to Maxey (1982), β has a typical value of 3.5 which does not depend on the altitude above the ground. Figure 8 shows that $L_{33}^{(x)}/L_{33}^{(y)}$ varies with height. An RDT calculation predicts that this ratio should increase with increasing

non-dimensional shear β. According to RDT, $L_{33}^{(x)}/L_{33}^{(y)} = 1.4$ corresponds to $\beta = 1.3$, 1.6 and 1.4 for $2p = 5/3$, 1 and 2.6, respectively; $L_{33}^{(x)}/L_{33}^{(y)} = 3$ corresponds to $\beta = 3.1$, 4.3 and 3.1 for $2p = 5/3$, 1 and 2.6, respectively. This is consistent with the evaluation $\beta = O(1)$ at all heights in the surface layer but two reasons may explain why $L_{33}^{(x)}/L_{33}^{(y)}$ increases with z. The shear S decreases with height and the spectrum varies in a non-trivial manner. The usual interpretation of β is $\beta = S\ell_e/u_e$ and $S = u_*/(k_0 z)$. If both the RDT and LES performed above are valid, $\ell_e = \beta k_0 z$ is the scale of large eddies, with βk_0 varying from 0.6 to 1.75.

5.2. *Comparison with the case of shear without blocking* (*free-stream turbulence*)

This case is simpler than the case of shear plus blocking, because the turbulence remains homogeneous. It can be deduced from the previous calculations by setting $z \to \infty$ (i.e. by dropping all the $e^{-\kappa z}$ terms), since the non-dimensionnal shear β does not depend on z in our calculation. Using (2.19) and (2.16) in the absence of blocking, $L_{33}^{(x)}/L_{33}^{(y)}$ becomes

$$\frac{L_{33}^{(x)}}{L_{33}^{(y)}} = \frac{\displaystyle\int\int \Phi_{33}^{H}(0, m_2, m_3)\,\mathrm{d}m_2\,\mathrm{d}m_3}{\displaystyle\int\int \left(\frac{m_1^2 + (m_3 + \beta m_1)^2}{m_1^2 + m_3^2}\right)^2 \Phi_{33}^{H}(m_1, 0, m_3 + \beta m_1)\,\mathrm{d}m_1\,\mathrm{d}m_3} \tag{5.3}$$

Using some algebra, we find that

$$\frac{L_{33}^{(x)}}{L_{33}^{(y)}} = \frac{\displaystyle\int_0^{2\pi} \sin^2\theta\,\mathrm{d}\theta}{\displaystyle\int_0^{2\pi} \frac{\sin^2\theta}{(1 - 2\beta\cos\theta\sin\theta + \beta^2\sin^2\theta)^2}\,\mathrm{d}\theta}$$

which shows that in a pure sheared situation and when a Kármán spectrum is used, the ratio $L_{33}^{(x)}/L_{33}^{(y)}$ does not depend of the spectrum decay $2p$, which is consistent with Townsend (1976). After a few more calculations, one can show that

$$\frac{\displaystyle\int_0^{2\pi} \sin^2\theta\,\mathrm{d}\theta}{\displaystyle\int_0^{2\pi} \frac{\sin^2\theta}{(1 - 2\beta\cos\theta\sin\theta + \beta^2\sin^2\theta)^2}\,\mathrm{d}\theta} = 1. \tag{5.4}$$

Thus one major finding of this calculation is that in a pure shear situation, $L_{33}^{(x)}/L_{33}^{(y)} = 1$. This is discussed below.

Based on the vertical velocity, one can conclude as follows for various situations: (i) in the case of shear without blocking, $L_{33}^{(x)}/L_{33}^{(y)} = 1$; (ii) in a pure blocking situation (without shear), $L_{33}^{(x)}/L_{33}^{(y)} = 1$ also ($\beta = 0$); (iii) in the presence of both shear and blocking $L_{33}^{(x)}/L_{33}^{(y)} > 1$.

The pure shear case (without blocking) was studied by Townsend (1970, 1976) and Hunt & Carruthers (1990) using RDT simulations. Hunt & Carruthers (1990) plotted the longitudinal velocity fluctuations u_1 which displayed elongated large eddies, whereas Townsend (1970) and Townsend (1976) calculated the correlation function and the integral length scales for u_1.

The fact that $L_{33}^{(x)}/L_{33}^{(y)} = 1$ while $L_{11}^{(x)}/L_{11}^{(y)} > 1$ in a pure shear RDT calculation can be explained by the loss of a major part of the redistribution of energy through the

Poisson equation for pressure,

$$-\Delta p = 2\frac{\partial U_l}{\partial x_m}\frac{\partial u_m}{\partial x_l} + \frac{\partial u_l}{\partial x_m}\frac{\partial u_m}{\partial x_l} = 2S\frac{\partial u_3}{\partial x_1} + \frac{\partial u_l}{\partial x_m}\frac{\partial u_m}{\partial x_l}, \tag{5.5}$$

subjected to appropriate boundary conditions, and where $\Delta = \nabla^2 = \partial^2/\partial x^2 + \partial^2/\partial y^2 + \partial^2/\partial z^2$, U_i is the mean velocity field and u_j the fluctuating field. Non-hydrostatic corrections in the pressure are thus determined mainly through the nonlinear term.

In the case of RDT for shear without blocking, the equations for u_1 and u_3 thus reduce to (neglecting the viscous term)

$$\left.\begin{aligned}\frac{\partial u_1}{\partial t} + Sz\frac{\partial u_1}{\partial x_1} &= \frac{\partial}{\partial x_1}\left[\Delta^{-1}\left(2S\frac{\partial u_3}{\partial x_1}\right)\right] - u_3 S,\\ \frac{\partial u_3}{\partial t} + Sz\frac{\partial u_3}{\partial x_1} &= \frac{\partial}{\partial x_3}\left[\Delta^{-1}\left(2S\frac{\partial u_3}{\partial x_1}\right)\right].\end{aligned}\right\} \tag{5.6}$$

This shows that in a pure shear (without blocking) situation, the coupling of the velocity equations is one way only. There is no influence of the distortion of u_1 on the third component u_3 (the contrary not being true). Therefore, structures created on u_1 by the distortion may have no counterpart on u_3.

On the other hand, it was shown by Carlotti (2001) that blocking RDT is in fact an application of the method of images, i.e. a symetrization of the vorticity field $\boldsymbol{\omega} = \nabla \times \boldsymbol{u}$. Therefore, in the presence of both shear and blocking, elongated large eddies apparent on the field u_1 are transferred to all the components of the fluctuating velocity field through induction (Biot and Savart's law).

The present calculation shows that the redistribution of energy among directions through blocking is a much more efficient process than through shear, even though sheared-and-blocked turbulence is further from isotropy than sheared turbulence.

From a pragmatic point of view, in the pure shear situation, elongated large eddies exist but they have no signature in the vertical velocity field. In the shear and blocking case, blocking redistributes the energy of the large eddies in a way which makes the signature of the structures apparent in the vertical velocity field.

6. Conclusion

In this study, estimates of inhomogeneous integral scales are derived from the mathematics of rapid distortion theory (RDT) for the case of wall-bounded high-Reynolds-number turbulence and from large-eddy simulation (LES) of a neutrally stratified atmospheric boundary layer (ABL). In homogeneous turbulence, a single integral scale can be defined, and it can be shown that it must be proportional to the main functional length scale of the flow, namely the dissipation scale. On the other hand, in inhomogeneous turbulence, the present paper shows that it is possible to introduce 24 different integral scale (eighteen scales $L_{ij}^{(x_k+)}$ and six scales $L_{ij}^{(z-)}$). In our analysis, we focused on the four length scales $L_{33}^{(x_i\pm)}$, because they are the most affected by blocking.

It is shown from RDT that the asymptotic behaviour of the integral length scales for small heights depends crucially on the spectrum power law $-2p$. Indeed, when $2p > 1$ there is always one length scale which does not scale with the distance to the wall z. Only the downward integral scale $L_{33}^{(z-)}$ is proportional to z for any $2p$.

The integral scale $L_{33}^{(z-)}$ is thus a good candidate to be interpreted as Prandtl's mixing length. This gives a way of estimating theoretically Kármán's constant, and we find a value between 0.2 and 0.5 depending on the spectrum decay $2p$.

These results show that the assumption, often made in studies of boundary layers, that all the lengths are proportional to z, is thus not compatible with the assumption of a spectrum decaying according to Kolmogorov's law, but rather with a spectrum following a -1 power law. This is an encouraging result since there is now widespread theoretical, experimental and numerical evidence that such a -1 power-law subrange exists in the spectra of high-Reynolds-number wall-bounded turbulence, for eddies larger than z. The RDT results allow the vertical profiles of the integral length scales computed from the LES outputs to be interpreted: above the third grid point, the vertical profiles of the integral length scales have a linear shape, as expected for high-Reynolds-number turbulence and $2p = 1$. Very close to the surface, the upward integral length scales decreases with z because of the fast decay of the spectrum ($2p > 2$) due to the LES subgrid model.

The longitudinal-to-transverse integral length scale ratio $L_{33}^{(x)}/L_{33}^{(y)}$ is computed using RDT and LES. This ratio is interpreted as the aspect ratio of elongated near-wall large eddies, which are ubiquitous features of LES of boundary layers in which shear plays an important role in the dynamics. The LES shows that $L_{33}^{(x)}/L_{33}^{(y)}$ is an increasing function of z, which, according to RDT, corresponds to β between 1 and 4, of the order of the theoretical value of 3.5 published by Maxey (1982). From RDT, the evolution with z of the longitudinal-to-transverse integral length scale ratio means either that the effective shear β and the spectral power law $2p$ vary in a non-trivial manner, or if both the RDT and LES are valid the scale of the large eddies is proportional to βz with β varying from 1.3 to about 4.

These findings on integral scales in the atmospheric boundary layer, found both through inhomogeneous RDT and LES, still have to be confirmed by field experiments, which may also shed more light on energy transfer processes associated with the anisotropic scaling of the integral scales.

The implications for LES subgrid models near walls are of importance. First, LES models based on a Boussinesq hypothesis (the hypothesis that small scales act in an isotropic way on the large scales) have to take our findings into account by a modification of the model close to the wall (see Redelsperger, Mahé & Carlotti 2001). Since nearly all LES models used nowadays rely explicitly or implicitly on the Boussinesq hypothesis (most of them through their origins as modified Smagorinski models, including the dynamic models), our results may explain the many problems found in taking into account near-wall turbulence. They also show that the assumptions used in the theory intended to correct some models (such as a $-5/3$ decay of the spectrum) might stand on a very weak basis. For the next generation of models, which will eventually discard the Boussinesq hypothesis and be based on anisotropic ideas, even at the subgrid scale, one solution to overcome the difficulties may be to assume anisotropy of the dissipation and not only of the subgrid kinetic energy.

The authors would like to thank the anonymous referees who helped to improve the manuscript significantly and J. C. R. Hunt, C. Cambon, J. P. Bertoglio, and J. L. Redelsperger for fruitful discussions. We would also like to thank C. Bastin for her help in dealing with equation (5.4). P. Carlotti is funded by the French ministère de l'équipement, du logement et des transports and P. Drobinski is funded by the Centre National de la Recherche Scientifique (CNRS). This research has been supported

by the Institut National des Sciences de l'Univers (INSU) through the Programme ATmosphère Océan à Multi-échelle (PATOM).

Appendix A. Lemma

In this Appendix, the lemmas used in the article are given for the sake of completeness. The proofs are not given, but can be found in mathematics textbooks or in Carlotti (2001).

LEMMA 1. *Let f be a differentiable function such that $\int f$ and $\int f'$ converge absolutely and that f is twice differentiable in 0. Then*

$$\lim_{A\to\infty}\int_0^\infty f(x)\frac{\sin(Ax)}{x}\,\mathrm{d}x = \frac{\pi}{2}f(0).$$

LEMMA 2. *Suppose f is integrable. Then*

$$\lim_{A\to\infty}\int_{-\infty}^{\infty} f(x)\cos Ax\,\mathrm{d}x = 0.$$

Appendix B. Theorems

In this Appendix, the theorems used in the article are given. The proofs can be found in Carlotti (2001).

THEOREM 1. *Let $0 < \alpha < 1$, d be the space dimension and*

$$I(l) = \int\cdots\int_{\mathbb{R}^d}\frac{f(\boldsymbol{x})K(l\boldsymbol{x})}{|\boldsymbol{x}|^\alpha}\,\mathrm{d}\boldsymbol{x}$$

so that

$$f(\boldsymbol{x}) = \sum_{j=0}^{N} f_j(\theta)r^{-j} + O_{r\to\infty}\left(r^{-(N+1)}\right),$$

$$K(\boldsymbol{x}) = \sum_{j=0}^{N-d} K_j(\theta)r^j + O_{r\to 0}(r^{N-d+1}),$$

where $\boldsymbol{x} = r\boldsymbol{\theta}$, $|\boldsymbol{\theta}| = 1$, $r \in \mathbb{R}^+$, then

$$I(l) = \sum_{j=0}^{N}\left(\mathrm{fp}\int\cdots\int_{\mathbb{R}^d}\frac{f_j(\boldsymbol{\theta})K(r\boldsymbol{\theta})}{r^{j-d+1+\alpha}}\,\mathrm{d}\boldsymbol{\theta}\,\mathrm{d}r\right)l^{j-d+\alpha} + \sum_{j=0}^{N-d}\left(\mathrm{fp}\int\cdots\int_{\mathbb{R}^d} f(r\boldsymbol{\theta})K_j(\boldsymbol{\theta})r^{j+d-1-\alpha}\,\mathrm{d}\boldsymbol{\theta}\,\mathrm{d}r\right)l^j + O_{l\to 0}(l^{N-d+1}).$$

THEOREM 2. *Let $\alpha = 0$, then the function $I(l)$ defined in Theorem 2 becomes*

$$I(l) = \int\cdots\int_{\mathbb{R}^d} f(\boldsymbol{x})K(l\boldsymbol{x})\,\mathrm{d}\boldsymbol{x}$$

and

$$I(l) = \sum_{j=0}^{N} \left(\mathrm{fp} \int \cdots \int_{\mathbb{R}^d} \frac{f_j(\boldsymbol{\theta}) K(r\boldsymbol{\theta})}{r^{j-d+1}} \, \mathrm{d}\boldsymbol{\theta} \, \mathrm{d}r \right) l^{j-d}$$
$$- \left(\iint K_{j-d}(\theta) f_j(\theta) \, \mathrm{d}\theta \right) l^{j-d} \ln l$$
$$+ \sum_{j=0}^{N-d} \left(\mathrm{fp} \int \cdots \int_{\mathbb{R}^d} f(r\boldsymbol{\theta}) K_j(\boldsymbol{\theta}) r^{j+d-1} \, \mathrm{d}\boldsymbol{\theta} \, \mathrm{d}r \right) l^j + O_{l\to 0}(l^{N-d+1} \ln l). \quad \text{(B 1)}$$

REFERENCES

Andrén, A. & Moeng, C. H. 1993 Single-point closures in a neutrally stratified boundary layer. *J. Atmos. Sci.* **50**, 3366–3379.

Batchelor, G. K. 1953 *The Theory of Homogenous Turbulence*. Cambridge University Press.

Carlotti, P. 2001 Distorted turbulence near rigid boundaries. PhD thesis, University of Cambridge.

Carlotti, P. 2002 Two point properties of atmospheric turbulence very close to the ground: comparison of a high resolution LES with theoretical models. *Boundary-Layer Met.* **104**, 381–410.

Carlotti, P. & Hunt, J. C. R. 2003 Developments in turbulence for aeronautical and other applications. In *Fluid Dynamics and Aeronautics: New Challenges* (ed. J. Périaux *et al.*), pp. 216–241. CIMNE, Barcelona.

Cuxart, J., Bougeault, P. & Redelsperger, J. L. 2000 A multiscale turbulence scheme apt for LES and mesoscale modelling. *Q. J. R. Met. Soc.* **126**, 1–30.

Deardorff, J. W. 1972 Numerical investigation of neutral and unstable planetary boundary layers. *J. Atmos. Sci.* **29**, 91–115.

Drobinski, P., Carlotti, P., Newsom, R. K., Banta, R. M., Foster, R. C. & Redelsperger, J.-L. 2004 The structure of the near-neutral surface layer. *J. Atmos. Sci.* **61**, 699–714.

Drobinski, P. & Foster, R. C. 2003 The origin of near-surface streaks in the neutrally-stratified planetary boundary layer. *Boundary-Layer Met.* **108**, 247–256.

Foster, R. C. 1997 Structure and energetics of optimal Ekman layer perturbations. *J. Fluid Mech.* **333**, 97–123.

Frisch, U. 1995 *Turbulence*. Cambridge University Press.

Högström, U. & Bergström, H. 1996 Organized turbulence structures in the near-neutral atmospheric surface layer. *J. Atmos. Sci.* **53**, 2452–2464.

Högström, U., Hunt, J. C. R. & Smedman, A. S. 2002 Theory and measurements for turbulence spectra and variances in the atmospheric neutral surface layer. *Boundary-Layer Met.* **103**, 101–124.

Hunt, J. C. R. & Carlotti, P. 2001 Statistical structure at the wall of the high Reynolds number turbulent boundary layer. *Flow, Turbulence, Combust.* **66**, 453–475.

Hunt, J. C. R. & Carruthers, D. J. 1990 Rapid distorsion theory and the 'problems' of turbulence. *J. Fluid Mech.* **212**, 497–532.

Hunt, J. C. R. & Graham, J. M. R. 1978 Free-stream turbulence near plane boundaries. *J. Fluid Mech.* **84**, 209–235.

Hunt, J. C. R., Moin, P., Lee, M., Moser, R. D., Spalart, P., Mansour, N. N., Kaimal, J. C. & Gaynor, E. 1989 Cross-correlation and length-scales in turbulent flows near surfaces. In *Advances in Turbulence 2* (ed. H. H. Fernholz & H. E. Fiedler). Springer.

Jacquin, L., Leuchtner, O., Cambon, C. & Mathieu, J. 1990 Homogeneous turbulence in the presence of rotation *J. Fluid Mech.* **220**, 1–52.

Kader, B. A. & Yaglom, A. M. 1989 Spectra and correlation functions of surface layer atmospheric turbulence in unstable thermal stratification. In *Turbulence and Coherent Structures* (ed. O. Métais & M. Lesieur), pp. 387–411. Kluwer.

Kaimal, J. C., Wyngaard, J. C., Izumi, Y. & Coté, O. R. 1972 Spectral characteristics of surface-layer turbulence. *Q. J. R. Met. Soc.* **98**, 563–589.

Lafore, J. P., Stein, J., Asencio, N. *et al.* 1998 The Meso-Nh atmospheric simulation system. Part I: adiabatic formulation and control simulation. *Ann. Geophys.* **16**, 90–109.

Lee, M. J. & Hunt, J. C. R. 1989 The structure of sheared turbulence near a plane boundary. In *Proc. Seventh Sympo. on Turbulent Shear Flow Stanford University, California, USA* (ed. P. R. Spalart).

Lin, C. L., Mc Williams, J. C., Moeng, C.-H. & Sullivan, P. P. 1996 Coherent structures in a neutrally-stratified planetary boundary layer. *Phys. Fluids* **8**, 2626–2639.

Lin, Z. C., Adrian, R. J. & Hanratty, T. J. 1996 A study of streaky structures in turbulent channel flow with particle image velocimetry. In *Proc. Eight Intl Symp. on Applied Laser Techniques to Fluid Mechanics, Lisbon, Portugal.*

Magnaudet, J. 2003 High Reynolds number turbulence in a shear free boundary layer: revisiting the Hunt-Graham theory. *J. Fluid Mech.* **484**, 167–196.

Mahrt, L. & Gibson, W. 1992 Flux decomposition into coherent structures. *Boundary-Layer Met.* **60**, 143–157.

Malkus, W. V. R. 1956 Outline of a theory of turbulent shear flow. *J. Fluid Mech.* **1**, 521–539.

Mann, J. 1994 The spatial structure of neutral atmospheric surface layer turbulence. *J. Fluid Mech.* **273**, 141–168.

Maxey, M. R. 1982 Distortion of turbulence in flows with parallel streamlines. *J. Fluid Mech.* **124**, 261–282.

Moeng, C.-H. & Sullivan, P. P. 1994 A comparison of shear- and buoyancy-driven planetary boundary layer flows. *J. Atmos. Sci.* **51**, 999–1022.

Moffatt, H. K. 1967 Interaction of turbulence with strong wind shear. In *Proc. URSI-IUGG Intl Colloq. on Atmospheric Turbulence and Radio Wave Propagation* (ed. A. M. Yaglom & V. I. Tatarski), pp. 139–154. Nauka, Moscow.

Morrison, J. F., Jiang, W., McKeon, B. J. & Smits, A. J. 2002 Reynolds number dependance of streamwise velocity spectra in turbulent pipe flow. *Phys. Rev. Lett.* **88**(21), 214501–214504.

Prandtl, L. 1952 *Essentials of Fluid Mechanics.* Blackie and Son Ltd.

Redelsperger, J.-L., Mahé, F. & Carlotti, P. 2001 A simple and general subgrid model suitable both for surface layer and free-stream turbulence. *Boundary-Layer Met.* **101**, 375–408.

Schmidt, H. & Schumann, U. 1989 Coherent structure of the convective boundary layer derived from large-eddy simulation. *J. Fluid Mech.* **200**, 511–562.

Townsend, A. A. 1970 Entrainment and the structure of turbulent flow. *J. Fluid Mech.* **41**, 13–46.

Townsend, A. A. 1976 *The Structure of Turbulent Shear Flows*, 2nd Edn. Cambridge University Press.

Weckwerth, T. M., Grund, C. J. & Mayor, S. D. 1997 Linearly-organized coherent structures in the surface layer. In *Proc. 12th Symp. on Boundary Layers and Turbulence, Vancouver, B.C., Canada.*

Wilczak, J. M. & Tillman, J. E. 1980 The three-dimensional structure of convection in the atmospheric surface layer. *J. Atmos. Sci.* **37**, 2424–2443.

Yaglom, A. M. 1991 Similarity laws for wall turbulence flows. In *New Approaches and Concepts in Turbulence* (ed. T. Dracos & A. Tsinober), pp. 387–411. Monte Verità, Birkhäuser.